Chemical Engineering Journal 454 (2023) 140144

Contents lists available at ScienceDirect

Chemical Engineering Journal

journal homepage: www.elsevier.com/locate/cej

Lithiophilic and conductive framework of 2D MoN nanosheets enabling planar lithium plating for dendrite-free and minimum-volume-change lithium metal anodes

De Gao [a], Shuzhen Deng [a,b], Xiaogang Li [c], Yingxi Zhang [a,e], Tuan Lv [a], Yang He [a], Weijian Mao [a], Hui Yang [c], Jingwei Zhang [d], Paul K. Chu [e], Kaifu Huo [a,*]

[a] Wuhan National Laboratory for Optoelectronics (WNLO), School of Optical and Electronic Information, Huazhong University of Science and Technology, Wuhan 430074, China
[b] China-EU Institute for Clean and Renewable Energy, Huazhong University of Science and Technology, Wuhan 430074, China
[c] Department of Mechanics, School of Aerospace Engineering, Huazhong University of Science and Technology, Wuhan 430074, China
[d] National & Local Joint Engineering Research Center for Applied Technology of Hybrid Nanomaterials, Henan University, Kaifeng 475004, China
[e] Department of Physics, Department of Materials Science and Engineering, and Department of Biomedical Engineering, City University of Hong Kong, Tat Chee Avenue, Kowloon, Hong Kong, China

ARTICLE INFO

Keywords:
Lithium metal
Anode
Molybdenum nitride
Lithiophilicity
Planar plating

ABSTRACT

Lithium (Li) is a promising anode for high-energy rechargeable batteries but its practical implementation is impeded by uncontrollable dendrite growth and huge volume changes. Herein, we report a dendrite-free Li composite anode with minimum volume change, which is composed of 3D interpenetrating Li and lithiophilic MoN nanosheets prepared by mechanical rolling and folding. The conductive 2D MoN nanosheets boasting excellent lithiophilic affinity and small lattice mismatch with Li induce planar Li plating therefore suppressing dendrite growth along the perpendicular direction. The MoN nanosheets interwoven framwork provides abundant Li accommodation sites and the horizontally plated Li fills the nanoscale gaps between the MoN nanosheets, thus minimizing volume change during cycling. Li_3N generated *in situ* by the surface reaction between MoN and Li enhances the ionic conductivity and interface stability. The Li-MoN anode shows a low Li plating overpotential of 15.0 mV and excellent stability for 2,500 h at 1 mA cm^{-2}. Paired with the $LiFePO_4$ cathode, the full cell shows 99.7 % Coulombic efficiency and 87.7 % capacity retention after 650 cycles at 170 mA g^{-1}. The results provide insights into the design of 3D host enabling planar Li plating for dendrite-free and minimum-volume-change Li metal anodes.

1. Introduction

The pursuit for high-energy–density batteries for portable electronic devices and electric vehicles (EVs) has spurred the development of high-capacity electrode materials [1–3]. Lithium (Li) is one of the promising anode materials especially for next-generation high-energy–density battery systems such as lithium-sulfur (Li-S) batteries due to the high theoretical specific capacity of 3860 mAh/g and low electrochemical potential of −3.04 V *vs* the standard hydrogen electrode [4–6]. Nevertheless, irregular Li electrodeposition generally causes the growth of Li dendrites during repetitive plating/stripping processes, consequently impaling the separator and causing internal short circuit, thermal runaway, and safety concerns [7–9]. Moreover, the high chemical activity of Li and large volume changes of the "hostless" Li metal anode cause repeated breakage and reconstruction of the fragile solid electrolyte interface (SEI) accompanied by continuous depletion of active Li and electrolyte during cycling, thereby giving rise to low Coulombic efficiency (CE) and inferior cycling stability [10,11]. Various strategies have been explored to suppress the growth of Li dendrites, for example, by adding electrolyte additives to build a dense SEI or engineering artificial SEI on Li anodes [12–16]. However, the planar Li metal anodes still undergo large volume changes during cycling especially at large areal capacities, significantly restricting the use of Li metal anodes [17,18]. Recently, three-dimensional (3D) Li metal composite anodes have been developed by confining Li in a scaffold/host to reduce volume change and enable low Li deposition overpotential due to the reduced

* Corresponding author.
E-mail address: kfhuo@hust.edu.cn (K. Huo).

https://doi.org/10.1016/j.cej.2022.140144
Received 27 August 2022; Received in revised form 18 October 2022; Accepted 29 October 2022
Available online 4 November 2022

local current density [18–20]. Different hosts or current collectors have recently been investigated for 3D Li metal composite anodes, for instance, Cu foams [19,21,22], Ni foams [23,24], and carbon frameworks [25,26]. However, the volumetric energy densities of these 3D nanostructured Li metal composite anodes are limited on account of the large volume fraction of the scaffolds. Moreover, Li is generally deposited on the surface of conductive current collectors rather than the inner host, especially at high current densities. Therefore, it is necessary to create abundant lithiophilic nucleation sites in order to incorporate Li into a 3D structured framework.

Theoretically, electrodeposition of Li on a substrate commences with heterogeneous nucleation and then homogeneous Li plating. Therefore, the surface properties of the substrate affect the Li electrodeposition. Archer et al. have reported that a conductive substrate with a small lattice mismatch with the deposited metal layers is beneficial to reversible metal plating/stripping [27]. Recently, 2D $Ti_3C_2T_x$-MXene nanosheets have been investigated as substrates to regulate Li/Na deposition due to the large surface, high conductivity, and low lattice mismatching with Li [28–30]. Yang et al. have reported that $Ti_3C_2T_x$ Mxene films can regulate horizontally grown pebble-like Li [29] and Wei et al. have shown that the $Ti_3C_2T_x$ MXene intermediate layer on the Cu foil facilitates Li planar growth by ionic bonding and lattice confinement [30]. Despite recent progress, $Ti_3C_2T_x$ MXene nanosheets usually have abundant functional groups such as −O, −OH, −F and these oxygen- and fluorine-terminated groups can react with Li to affect Li nucleation and palting [28–30]. Recently, nanostructured molybdenum nitrides such as MoN and Mo_2N have been investigated as electrode materials or scaffolds for electrochemical energy storage because of the large specific surface area and high electrical conductivity [31–33]. Similar to $Ti_3C_2T_x$ MXene, 2D MoN nanosheets with a hexagonal surface structure have excellent lithiophilicity and a low lattice mismatching with Li, but do not contain abundant surface oxygen and fluorine terminations. Although they are promising substrates for regular and planar Li electrodeposition, heterogeneous nucleation and planer plating of Li on 2D MoN nanosheets have not reported.

Herein, the 2D MoN nanosheets are utilized to guide Li planar deposition, suppress dendrite growth, and minimize the volume change for advanced Li metal anodes. The Li-MoN composite anode consisting of 3D interpenetrated Li metal and lithiophilic MoN nanosheets is prepared by a simple mechanical rolling and folding method. The resulting Li-MoN composite anode has several advantages. Firstly, 2D MoN nanosheets facilitate planar Li deposition on the surface of MoN as a result of the excellent lithiophilicity and low lattice confinement with Li, consequently mitigating Li dendrite formation by preventing Li growth along the perpendicular direction. Secondly, 2D MoN nanosheets interwoven framework offers Li accommodation sites and the horizontally plated Li fills the nanoscale gaps betweens the MoN nanosheets to retain minimum volume change during cycling. Thirdly, the Li-MoN hybrid anode facilitates fast electron/ion transport and reduces the local current density due to the high conductivity and large surface area. Moreover, the abundant interfaces between Li and MoN nanosheets produce small interface impedance to attain the high-rate capability. Fourthly, the highly Li^+ conductive Li_3N and Mo generated *in situ* by the surface reaction of MoN and Li synergistically result in high ionic conductivity and excellent interface stability. The Li-MoN composite anode shows a low overpotential of 15 mV at 1 mA cm^{-2} and long cycling lifetime of 2,500 h at 1 mA cm^{-2} with a capacity of 1 mAh cm^{-2}. When the current density is increased to 10 mA cm^{-2} with a fixed capacity of 5 mAh cm^{-2}, the symmetrical cell with the Li-2D MoN electrodes still delivers excellent cycling performance showing a lifespan of 600 h. By pairing it with the $LiFePO_4$ cathode, the full cell composed of $LiFePO_4$// Li-MoN has excellent cycling characteristics and rate capability revealing large potential in high-energy Li metal batteries.

2. Experimental section

2.1. Sample preparation

In the preparation of MoN nanosheets, molybdenum sulfide (Aladdin, 1.05 g) and sodium carbonate (Aladdin, 0.625 g) were mixed and heated to 750 °C for 3 h under ammonia. The product was immersed in 3 % HCl solution to remove the Na_2S by-product and the MoN nanosheets powder was obtained after vacuum freeze-drying.

The Li-2D MoN anode was fabricated by a facile calendaring and folding strategy. The as-synthesized 2D MoN nanosheets were dispersed onto the surface of the Li foil and then rolled with the Li foil to form an elongated composite foil in an Ar-filled glove box (O_2 and $H_2O < 0.1$ ppm). It was folded from the middle and then rolled again. During the subsequent rolling process, the MoN nanosheets were embedded or attached tightly onto the surface of Li. The folding and calendaring operation was repeated several times to produce the lamellar Li-2D MoN film electrode in which metallic Li was confined in the MoN nanosheets integrated framework with strong affinity and abundant interfaces. Typically, the folding and rolling process was carried out for 8 times to produce the layered Li-MoN composite plate and the content of MoN nanosheets in the composite electrode was about 50 wt%. The Li-MoN composite plate was cut into disks with a diameter of 12 mm for testing of the symmetric cells and full cells.

2.2. Materials characterization

Field-emission scanning electron microscopy (FE-SEM, Nano-SEM450) and transmission electron microscopy (TEM, TecnaiG20) were conducted to characterize the morphology of the MoN nanosheets, Li foil, and Li-MoN composite anode. The chemical states of MoN and Li-MoN were determined by X-ray photoelectron spectroscopy (XPS, AXIS-ULTRADLD-600 W) and the structure was analyzed by X-ray diffraction (XRD, Philips X'Pert Pro). The thickness of the 2D MoN nanosheet was determined by atomic force microscopy (AFM, SPM9700).

2.3. Electrochemical evaluation

The CR2025 coin cells were assembled in an Ar-filled glove box (O_2 and $H_2O < 0.1$ ppm) for both the symmetrical cells and full batteries. In the symmetrical cells, the cathode and anode were the same bare Li foil or Li-MoN composite foil. The electrolyte was 1 M lithium bis(trifluoromethane sulfonyl)imide (LiTFSI) dissolved in 1, 3-dioxolane (DOL) and 1, 2-dimethoxyethane (DME) (1:1 by volume ratio) with 2.0 wt% $LiNO_3$ as the additive. The full cells were assembled with the Li-MoN composite anode or bare Li anode and $LiFePO_4$ plate as the cathode. The electrolyte was 1 M $LiPF_6$ in EC:DEC = 1:1 vol%.

The $LiFePO_4$ cathode was prepared by slurry coating and doctor blading method. The $LiFePO_4$ powder was mixed with super P conductive additive and polyvinylidene difluoride binder with a mass ratio of 8:1:1. The mass loading of $LiFePO_4$ was around 3.5 mg cm^{-2} and a polypropylene film (Celgard, 2400) was used as the separator in the batteries. Each coin cell contained around 60 μL of the electrolyte. The cycling characteristics of the symmetrical cells and full batteries were determined using the Neware testing instrument. The full cells were galvanostatically cycled between 2.5 and 4.2 V and electrochemical impedance spectroscopy, (EIS) was carried out on the CHI660D electrochemical workstation at frequencies between 100 kHz and 10 mHz.

2.4. Theoretical calculation

The Vienna *ab initio* package (VASP) was employed to perform the density-functional theory (DFT) calculation within the generalized gradient approximation (GGA) using the Perdew-Burke and Enzerhof (PBE) formulation [34,35]. The projected augmented wave (PAW)

potentials were applied to describe the ionic cores and valence electrons were counted using a plane wave basis set with a kinetic energy cutoff of 450 eV [36]. Partial occupancies of the Kohn–Sham orbitals were allowed using the Gaussian smearing method with a width of 0.05 eV. The electronic energy was considered self-consistent when the energy change was smaller than 10^{-4} eV. Geometrical optimization was considered convergent when the force change was smaller than 0.03 eV/Å. The Grimme's DFT-D3 methodology was utilized to describe the dispersion interactions. The equilibrium lattice constants of Li_3N and Li_3N/Mo structures were optimized using the $2 \times 2 \times 1$ Monkhorst-Pack k-point grid for Brillouin zone sampling.

3. Results and discussion

3.1. Design and fabrication of the Li-2D MoN composite anode

The Li-2D MoN anode is fabricated by a facile calendaring and folding strategy schematically illustrated in Fig. 1a. The ultra-thin MoN nanosheets are prepared from bulk MoS_2 by Na_2CO_3-assisted thermal nitriding under NH_3. The SEM, TEM and AFM images (Figs. S1a–c) show that the nanosheets have the sizes of 500–1,000 nm and an average thickness of 6.4 nm. XRD (Fig. S2a) and XPS (Fig. S2b and c) results further validate successful preparation of 2D MoN nanosheets. The three diffraction peaks at 31.9°, 36.2° and 49.0° are assigned to the (002), (200) and (202) planes of hexagonal MoN (JCPDS No.25–1367). The high-resolution XPS peaks at 232.1 and 228.9 eV are associated with Mo $3d_{3/2}$ and Mo $3d_{5/2}$ of Mo−N in MoN [31]. Different from 2D $Ti_3C_2T_x$ MXene with abundant oxygen and fluorine terminations, the 2D MoN nanosheets are free of fluorine functionality and the weak Mo−O peak arises from surface oxidation. The as-synthesized 2D MoN nanosheets are dispersed onto the surface of a Li foil and then rolled with the Li foil to form an elongated composite foil in an Ar-filled glove box. It is folded from the middle and then rolled again to increase association between the MoN nanosheets and Li. The folding and calendaring operations are repeated several times to produce the lamellar Li-2D MoN film electrode in which Li is confined into the MoN nanosheets integrated framework with strong affinity and abundant interfaces. Fig. 1b shows the optical photograph of the Li-MoN anode with a diameter of 12 mm after punching and the metallic color of Li is clearly observed. The FE-SEM image (Fig. 1c) demonstrates that the surface of Li-MoN electrode is relatively smooth and ultra-thin nanosheets are uniformly dispersed into the Li-2D MoN composite electrode. The cross-section SEM image

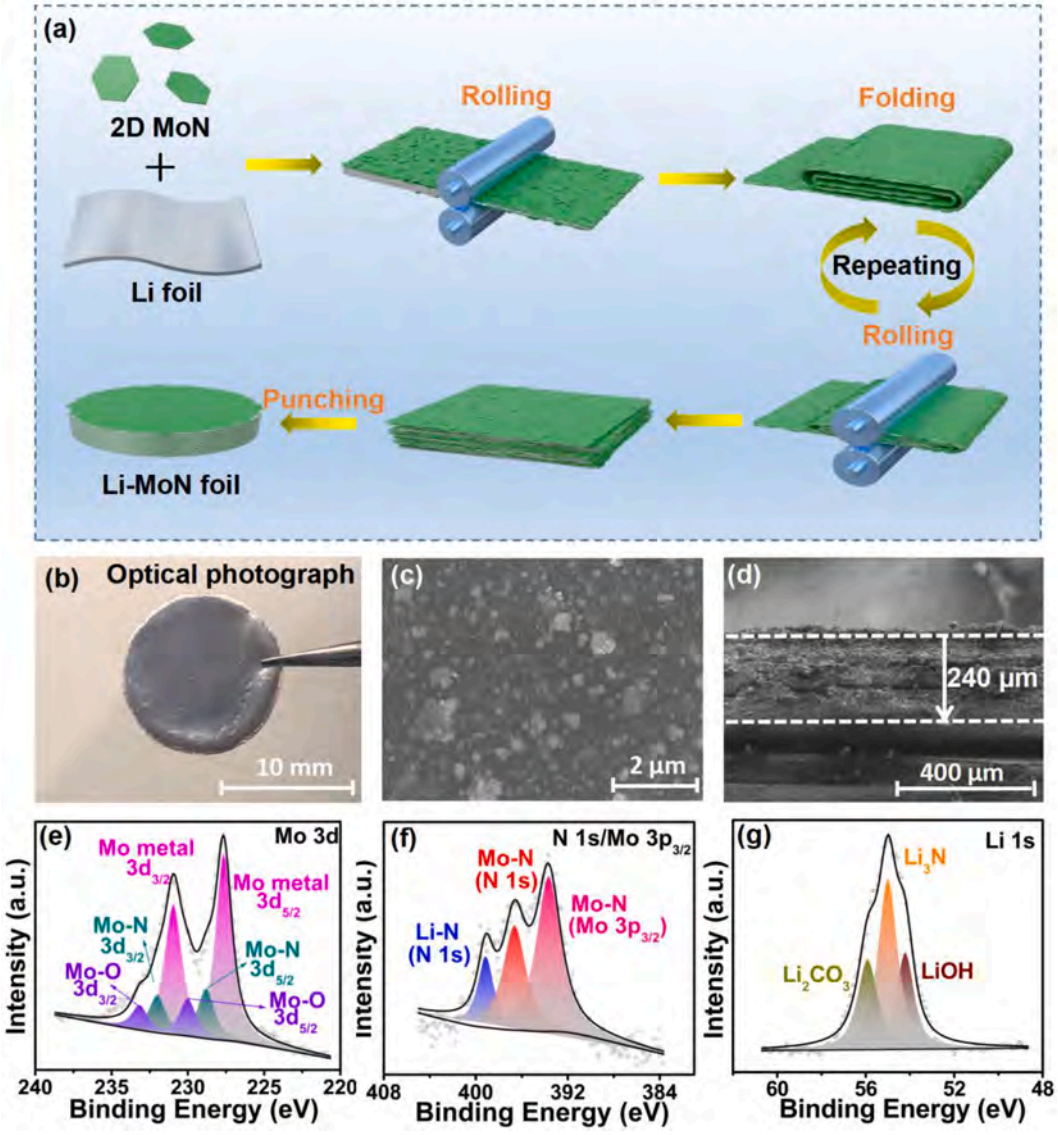

Fig. 1. (a) Schematical diagram of the fabrication process of the Li-2D MoN composite anode; (b) Optical photograph; (c) Top-view SEM and (d) Cross-sectional SEM images of the Li-MoN composite electrode; High-resolution XPS spectra of (e) Mo 3*d*, (f) N 1 *s*, and (g) Li 1 *s* acquired from the Li-2D MoN composite electrode.

(Fig. 1d) shows that the thickness of the Li-MoN anode is about 240 μm. The magnified cross-section SEM image (Fig. S3) discloses metallic Li is uniformly dispersed between MoN layers forming interconnected multilayered structure. The surface chemical states of the Li-MoN hybrid electrode are analyzed by XPS. As shown in Fig. 1e, the peaks at 232.1 and 228.9 eV are those of Mo $3d_{3/2}$ and Mo $3d_{5/2}$ of Mo−N in MoN, respectively. Two new peaks at 230.9 and 227.7 eV corresponding to Mo $3d_{3/2}$ and Mo $3d_{5/2}$ of metallic Mo appear [31]. Mo−O stems from surface oxidation during sample transfer in air prior to XPS. The high-resolution N 1 *s* peak at 399.2 eV reflects Li−N which is further confirmed by the Li 1 *s* peak at 55.1 eV of Li−N in Li_3N in Fig. 1g [12,31]. In the N 1 *s* spectrum, the Mo $3p_{3/2}$ peak overlaps partially with the N 1 *s* peak and peaks of Mo $3p_{3/2}$ of Mo−N in MoN also appear. The presence of Mo and Li_3N in the XPS results suggests that MoN can react with Li to form Li_3N and Mo (MoN + Li → Li_3N + Mo) at the contact interface during repetitive rolling-folding process. MoN has strong affinity with metallic Li and *in situ* formation of Li_3N gives rise to low interface impedance [31] and excellent electrochemical characteristics to be discussed later.

3.2. Theoretical calculations for planar plating

The XRD pattern of the Li-MoN composite electrode in Fig. 2a can be indexed to hexagonal MoN (JCPDS No. 25–1367) and cubic Li (JCPDS No. 15–0401). Although XPS indicates the presence of Li_3N and Mo, the diffraction peaks of Li_3N or metal Mo cannot identified, suggesting that only small amounts of Li_3N and Mo are formed by the surface reaction between Li and MoN. Although the XRD patterns of MoN in MoN nanosheets powder and Li-MoN electrode show the same peak positions, the MoN (002) lattice plane peak intensity in Li-MoN becomes stronger and the diffraction peak intensity of MoN (200) decreases sharply. For 2D MoN nanosheet, the top and bottom faces of 2D MoN nanosheets are enclosed by the (002) planes and the side face is (200) plane. Fig. S4a discloses that the Li-MoN composite foil exhibits larger ratio of $I_{(002)}/I_{(200)}$ compared with 2D MoN nanosheets power (1.46 and 0.33 for Li-MoN and 2D MoN nanosheets powder), suggesting that MoN nanosheets are mainly parallel to the direction of flat foil by the repeated mechanical calendaring. To confirm that the MoN nanosheets could be parallelly aligned by mechanical calendaring, we coat MoN nanosheets onto the Cu foil by a simple blade method followed by mechanical calendaring. The XRD pattern of the MoN/Cu foil (Fig. S4b) also shows a sharp increase in $I_{(002)}/I_{(200)}$ compared to the MoN nanosheets powder. Therefore, it is convincing to state that MoN nanosheets in Li-MoN are parallel to the direction of flat foil by the repeated mechanical calendaring.

The adsorption energies (E_{ad}) of Li on MoN, Li_3N, and Mo substrate with different crystalline planes are calculated by density function theory (DFT) simulation. The results are summarized in Fig. 2b and the adsorption structures are presented in Fig. S5. The E_{ad} values of Li atoms adsorbed on Li (110) and Li (200) are calculated to be −1.93 and −1.85 eV. However, MoN (002) and MoN (200) show larger E_{ad} for Li of −5.05 and −3.53 eV, respectively. The strong interaction between Li and MoN (002) lattice plane facilitates adsorption and nucleation of Li on the 2D MoN nanosheets [30,31]. Additionally, the adsorption energies of Li on Li_3N (−2.95 eV) and Mo (−2.93 eV) are lareger compared to Li on the Li substrate, suggesting that Li_3N and Mo generated *in situ* on the MoN surface could further lower the nucleation overpotential.

Bader charge analysis is further conducted to reveal the relationship between Li and different substrates (Fig. S6). A fraction of the Li charge density (charge = + 0.73 eV) is transferred to the surface of MoN to confirm the strong affinity between Li and MoN. The Li deposition properties on the (002) plane of MoN is schematically depicted in

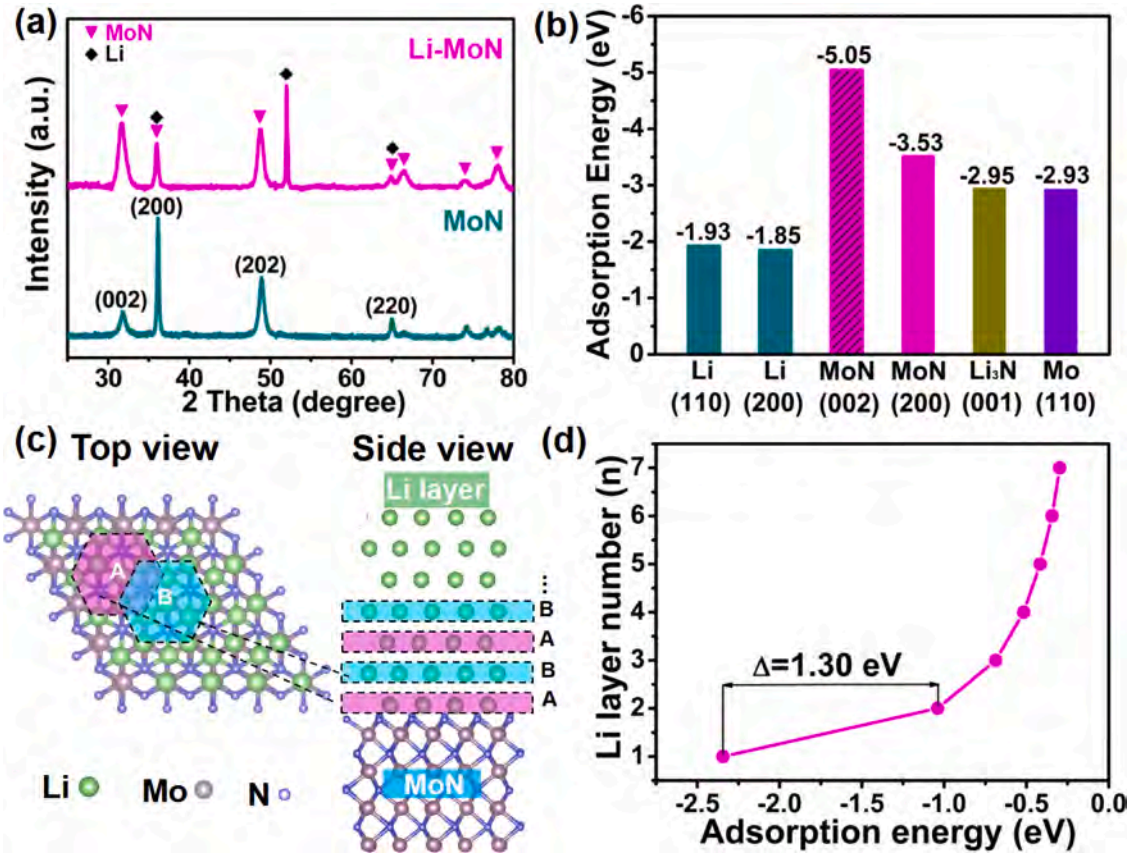

Fig. 2. (a) XRD patterns of the MoN nanosheets and Li-MoN composite anode; (b) Adsorption energy of Li atoms on different planes of metal Li, MoN, Li_3N and Mo; (c) Theoretical modeling of Li deposition on MoN (002); (d) E_{ad} of Li on MoN (002) as a function of the number of deposited layers (n).

Fig. 2c. MoN has a hexagonal unit cell comprising N and Mo layers stacked in the sequence of *N*-Mo-*N*-Mo-N. When Li is deposited on MoN (0 0 2), the first layer of Li is plated on the N atoms (A site). After all the A sites are covered by Li, subsequent Li atoms are deposited on the B sites (above the Mo atoms) forming a hexagonal layer. Therefore, hexagonal close-packed (hcp) Li layers with a coordination number of 6 are formed on the hexagonal lattice of MoN (0 0 2) plane and it is different from Li atoms on bulk Li metal with a coordination number of 8 [30]. The deposited hcp Li and MoN have the silimiar hexagonal crystal system (space group: $P6_3/mmc$) with low lattice mismatches of 1.6 % and 4.5 % for the a and b axes between the MoN (0 0 2) and Li (0 0 2) planes (Fig. S7 and Table S1). The relatively low lattice mismatch and excellent lithiophilic affinity enables epitaxial deposition of Li on 2D MoN nanosheets, resulting in dense and planar Li growth. Fig. 2d shows the adsorption energy of the Li layer on MoN as a function the number of deposited layers (n). The difference in E_{ad} between the first and second Li layer is about 1.3 eV. The large energy difference indicates that a new hcp-Li layer cannot be formed until the underlying layer is fully covered by Li [30]. Hence, the hcp-Li layers are deposited epitaxially on the MoN nanosheets and the transition hcp-Li layers provide the perfect foundation for further deposition of bcc-Li, resulting in a low deposition overpotential and planar Li plating.

3.3. Electrochemical characteristics

To evaluate the electrochemical performance of the Li-MoN composite electrode, symmetrical cells with two identical electrodes are assembled and assessed. The electrolyte is 1 M lithium bis (trifluoromethane sulfonyl)imide (LiTFSI) dissolved in 1, 3-dioxolane (DOL) and 1, 2-dimethoxyethane (DME) (1:1 by volume ratio) with 2.0 wt% $LiNO_3$ as the additive. For comparison, the electrochemical properties of the bare Li foil are also investigated. Fig. 3a shows the voltage profiles as a function of time for the symmetrical cells of Li-MoN//Li-MoN and the Li//Li counterparts at a current density of 1.0 mA cm^{-2} with a capacity of 1 mAh cm^{-2}. The Li-MoN composite anode exhibits long-term cycling stability for over 2,500 h with a smooth and small polarization potential of 15 mV (Fig. 3b). However, the Li//Li symmetrical cell shows fluctuating overpotentials over 75 mV and is short-circuited after cycling for 700 h. When the current density is increased to 10 mA cm^{-2} with a fixed capacity of 5 mAh cm^{-2}, the symmetrical cell composed of the Li-MoN electrodes still shows excellent cycling characteristics and a long life time of 600 h. However, the symmetrical battery with the pure Li foil shows severely fluctuating overpotentials and short-circuits after 320 h. The detailed comparison of the overpotentials is presented in Fig. 3b and d. The symmetrical cell of Li-MoN//Li-MoN shows a lower overpotential than the Li//Li counterpart.

The rate performance of the symmetrical cells of Li-MoN//Li-MoN and the Li//Li counterparts are investigated at different current densities with a fixed capacity of 1 mAh cm^{-2}. As shown in Fig. 3e and Fig. S8, the symmetrical cell of Li-MoN//Li-MoN exhibits much lower overpotentials than the symmetrical cell of Li//Li at different current densities. When the current density is increased from 0.5 to 5 mA cm^{-2}, the symmetrical cell of Li-MoN//Li-MoN has steady polarization voltages of 21.0, 28.8, 65.0, and 95.1 mV at current densities of 0.5, 1, 3 and 5 mA cm^{-2}, respectively. When the current density is reverted back to 1

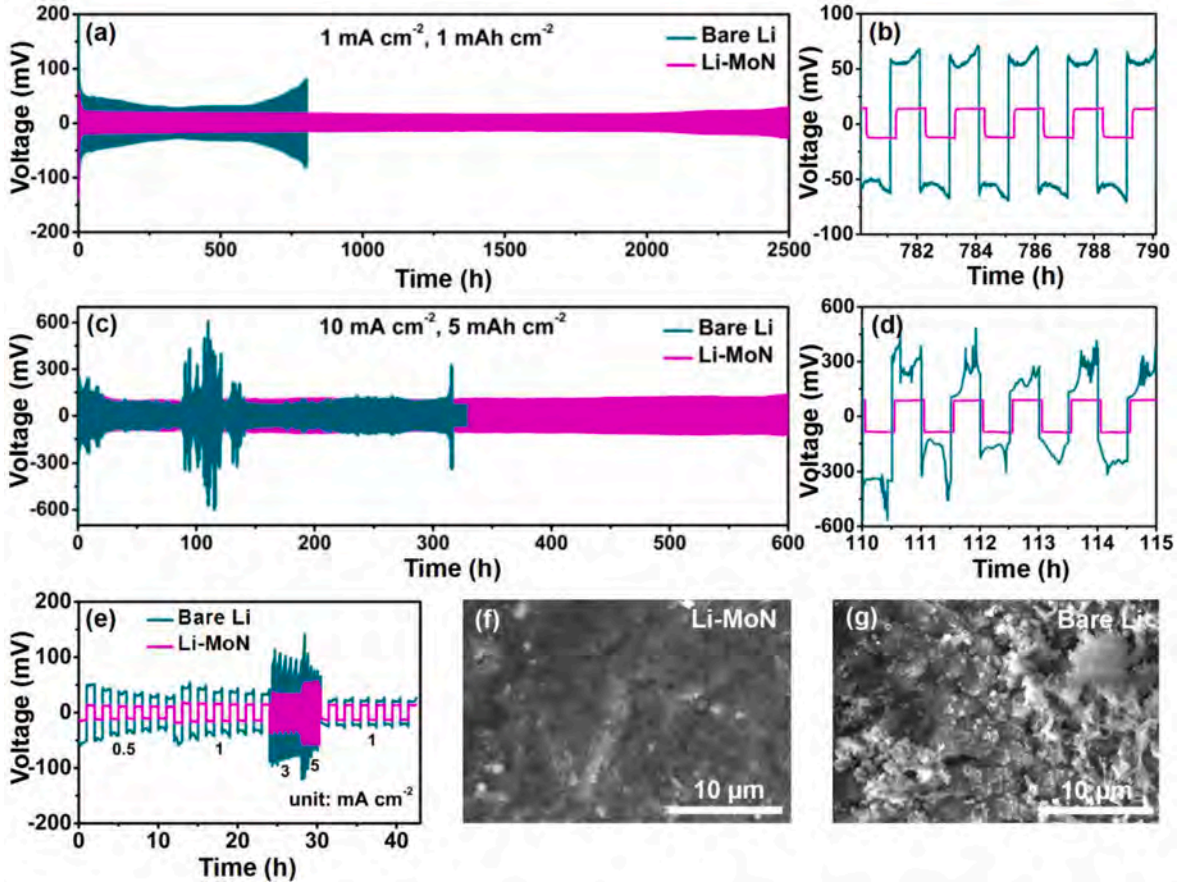

Fig. 3. Cycling performance of the symmetrical cells composed of the bare Li anode or Li-MoN composite anode. Voltage profiles of the symmetrical cells at 1 mA cm^{-2} with the capacity of 1 mAh cm^{-2} (a) and 10 mA cm^{-2} with the capacity of 5 mAh cm^{-2} (c); (b) and (d) Enlarged images of comparison of the overpotentials in (a) and (c); (e) Rate performance of the symmetrical cells at current densities from 0.5 to 5 mA cm^{-2} with the capacity of 1 mAh cm^{-2}; Top-view SEM images of (f) Li-MoN and (g) bare Li anodes after the cycling test.

mA cm^{-2}, the polarization voltage shows a smaller value of 26.5 mV. In contrast, the symmetrical cell of Li//Li shows much higher polarization voltages of 54.3, 84.9, 172.1, and 212.9 mV at current densities of 0.5, 1, 3 and 5 mA cm^{-2}, respectively. The poor characteristics of the symmetrical Li battery and large polarization voltage (Fig. S8) result from the large volume change, growth of dendritic Li, and accumulation of dead Li. The morphological evolution of the Li-MoN composite and pure Li after electrochemical cycling is examined by SEM. As shown in Fig. 3f and g, Li-MoN composite electrode has a smooth and uniform surface without any dendritic Li, and the cross-sectional SEM image indicates that the composite anode retains the multi-layered structure (Fig. S9a and b). On the contrary, the bare Li anode has a coarse and porous surface and Li dendrites can be clearly identified from the top-view and side-view SEM images (Fig. 3g and S9, d). EIS is carried out to compare the interface impedance of the bare Li and Li-MoN composite anode after different cycles. As shown in Fig. S10, Li-MoN shows lower interface impedances of 46.8, 6.7, 3.9, 1.2, and 2.1 Ω after 0, 5, 50, 100, and 300 cycles, respectively, which are smaller than those of bare Li anodes, indicating a more stable interface and faster Li$^+$ transport.

The Li plating/stripping behavior of the Li-MoN composite electrode and bare Li electrode is evaluated by high area capacity stripping and plating (Fig. 4). The top-view SEM images (Fig. 4g and h) of the Li foil shows obvious pores after Li stripping. After replating Li, Li clusters appear and grow rapidly into irregular bulges with a thick SEI. The loose interphase consumes active Li and electrolyte, undoubtedly bringing detrimental effects to Li$^+$ diffusion and contributing significantly to the generation of electrochemically "dead Li" and ultimately poor cycle performance. In contrast, the Li-MoN exhibits a relatively smooth and flat surface after Li stripping/plating. The surface of the Li-MoN anode becomes coarse after stripping 6 mAh cm^{-2} of Li due to exposure of 2D MoN nanosheets (Fig. 4b). After replating 6 mAh cm^{-2} of Li, the SEM image (Fig. 4c)of the Li-MoN anode shows a smooth surface without dendritic Li growth.

The volume stability of Li-MoN is investigated by thickness measurement after lithium stripping/plating. The thickness of Li decreases sharply from 436 to 406 μm after stripping 6 mAh cm^{-2} of Li, which increases to 450 μm after replating 6 mAh cm^{-2} of Li. However, the thickness of Li-MoN does not change obviously after stripping/plating with 6 mAh cm^{-2} of Li at 1 mA cm^{-2} and the cross-section SEM images (Fig. 4d-f) reveal the Li-MoN electrode retains the integrated layered

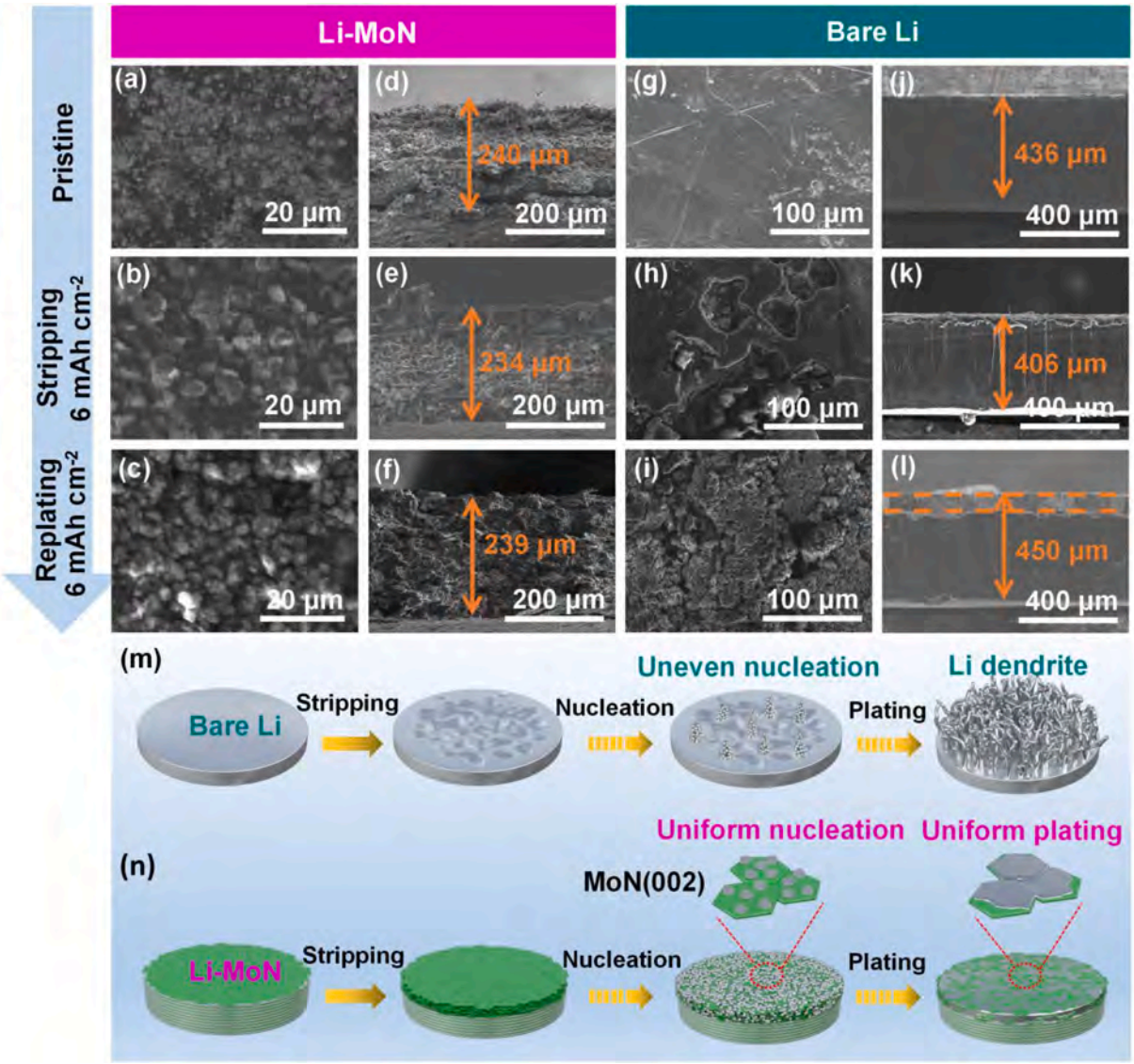

Fig. 4. (a) Top-view and (d) cross-sectional SEM images of the pristine Li-MoN anode, (b, e) Li-MoN anode after Li stripping of 6 mAh cm^{-2}, and (c, f) Li-MoN anode re-plated with Li of 6 mAh cm^{-2}; (g) Top-view and (j) Cross-section SEM images of bare Li, (h, k) Li anode after Li stripping of 6 mAh cm^{-2} and (i, l) Li anode re-platied with Li of 6 mAh cm^{-2}. The schematic of Li stripping/plating on (m) bare Li and (n) Li-MoN composite anode.

structure before and after stripping/plating cycling. We also investigate the morphology change of Li-MoN composite anode at the higher capacity of Li stripping/plating. The cross-section SEM of Li-MoN composite anode after stripping 12 mAh cm^{-2} of Li (Fig. S11) shows the thickness has no obvious change, however, the porous structure is observed, further confirming the Li filling with the gaps between MoN nanosheets. The schematics of the Li stripping and plating process of the Li and Li-MoN electrodes are schematically shown in Fig. 4m and n. The pure Li foil shows nonuniform stripping, nucleation, plating, and massive dendritic Li formation during repetitive Li plating and stripping. In contrast, the Li-MoN anode experiences a small thickness change without Li dendrite growth. The 2D MoN nanosheets framework acts as a stable skeleton and provides good Li ions and electron conductivity during Li stripping/plating due to good Li affinity and low lattice mismatching with Li. The MoN nanosheets with exposed (0 0 2) planes guide planar Li plating and stripping (Fig. 4n). The plated Li is electrochemically deposited on the surface of the MoN nanosheets and fills the nanogap between the MoN nanosheets. It not only effectively avoids the growth of Li dendrites on the electrode surface during cycling, but also maintains a minimum volume change.

To investigate the potential application of the Li-MoN anode, a full cell is assembled with the $LiFePO_4$ cathode (Li-MoN//LFP). For comparison, batteries are assembled with Li metal as the anode for the same anode/cathode capacity ratio. Fig. 5a presents the long-term cycling stability of the full cells at 1C (1C = 175 mA g^{-1}) in the voltage range of 2.5–4.2 V. The Li-MoN//LFP battery has superior cycling characteristics with 87.7 % capacity retention and 99.7 % CE after 650 cycles. In contrast, the Li//LFP battery suffers from sharp capacity fading after 300 cycles and short circuits occurs suddenly after 350 cycles. Fig. 5b and Fig. S12 show the rate capability of the full cells. The discharging capacities of Li-MoN//LFP are 97 mA h g^{-1} at 2C and 45 mA h g^{-1} at 5C, which are higher than those of the Li//LFP. The EIS curves (Fig. 5c) indicate that Li-MoN//LFP battery has smaller charge transfer impedance of 65.3 Ω compared with 233.3 Ω for Li//LFP, implying lower interface impedence and faster Li^+ diffusion in Li-MoN. The EIS curves of the Li-MoN//LFP and Li//LFP batteries after rate cycling also reveal

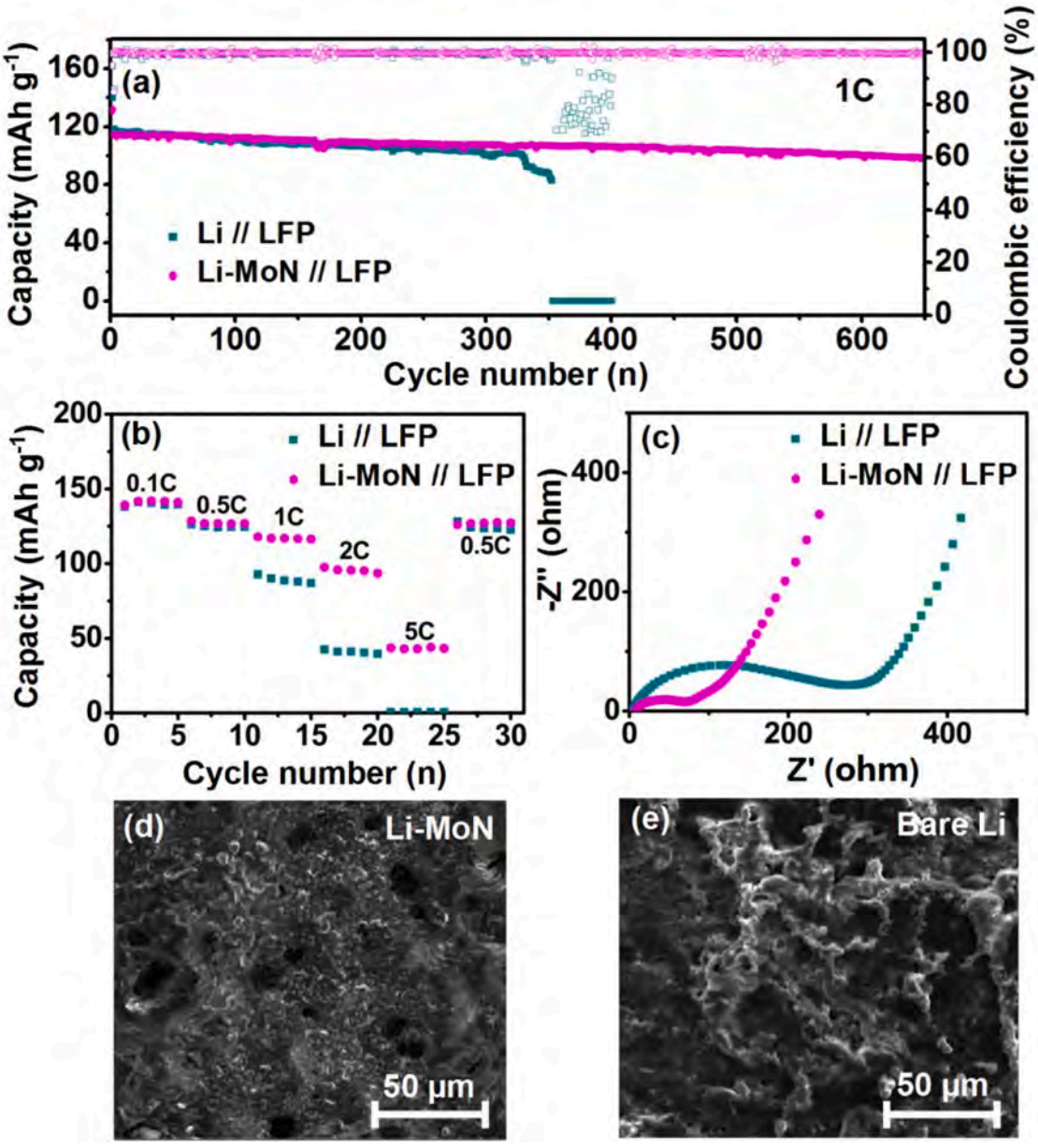

Fig. 5. (a) Long-term cycling of the Li-MoN//LFP and Li//LFP batteries at 1C; (b) Rate capability and (c) EIS curves of the Li-MoN//LFP and Li//LFP batteries; SEM images of Li-MoN anode (d) andLi anode (e) after 30 cycling test.

smaller charge transfer impedance for the Li-MoN//LFP battery (Fig. S13). To further confirm the superiority of Li-MoN anode, the Li-MoN and bare Li anodes after rate cycling are observed by SEM (Fig. 5d and e). The Li-MoN electrode has a relatively smooth surface without Li dendrite growth, however, the Li anode has a rough surface and shows obvious dendritic Li formation. The enhanced kinetics and improved reversibility of the Li-MoN anode suggest great potential of the Li-MoN anode in next-generation high-energy Li metal batteries.

4. Conclusion

A 3D dendrite-free Li-MoN composite anode is designed and demonstrated for advanced Li metal batteries. The MoN nanosheets with the exposed (0 0 2) plane have strong lithiophilic affinity and low lattice mismatching with Li consequently decreasing the nucleation barrier and facilitating planar Li nucleation and plating, which effectively avoids vertical growth of Li dendrites during cycling. The plated Li is electrochemically deposited on the surface of the MoN nanosheets and then fills the nanogap between the MoN nanosheets to achieve minimum volume change. Moreover, the large surface area of the MoN nanosheets decreases the local current density. The symmetrical cell comprising the Li-MoN electrode delivers excellent electrochemical performance such as a low overpotential of 15.0 mV at 1 mA cm^{-2} and robust cycling stability for 2,500 h. Compared with the Li anode, the Li-MoN anode has better rate capability and lower interface impedance. The full cell composed of the Li-MoN anode and $LiFePO_4$ cathode shows good cyclic characteristics and rate capability. The results provide insights into the design of 3D Li composite anodes with the transition metal nitrides as hosts for next-generation high-performance Li metal batteries.

Declaration of Competing Interest

The authors declare that they have no known competing financial interests or personal relationships that could have appeared to influence the work reported in this paper.

Data availability

Data will be made available on request.

Acknowledgements

This work was financially supported by National Natural Science Foundation of China (Nos. U2004210, 21875080 and 51572100), Shenzhen Municipal Science and Technology Innovation Commission (JCYJ20210324141613032), Innovative Research Group Project of the Natural Science Foundation of Hubei Province (2019CFA020), Special Projects for Local Science and Technology Development Guided by the Chinese Central Government (2019ZYYD024), City University of Hong Kong Strategic Research Grant (SRG 7005505), Shenzhen-Hong Kong Innovative Collaborative Research and Development Program (SGLH20181109110802117 and CityU 9240014), and City University of Hong Kong Donation Research Grant (DON-RMG No. 9229021). The authors are grateful to the facility support provided by the Analytical and Testing Center of HUST.

Appendix A. Supplementary data

Supplementary data to this article can be found online at https://doi.org/10.1016/j.cej.2022.140144.

References

[1] X.B. Cheng, R. Zhang, C.Z. Zhao, Q. Zhang, Toward safe lithium metal anode in rechargeable batteries: a review, Chem. Rev. 117 (2017) 10403.
[2] J. Zheng, M.S. Kim, Z. Tu, S. Choudhury, T. Tang, L.A. Archer, Regulating electrodeposition morphology of lithium: towards commercially relevant secondary Li metal batteries, Chem. Soc. Rev. 49 (2020) 2701.
[3] X. Shen, X. Zhang, F. Ding, J. Huang, R. Xu, X. Chen, C. Yan, F. Su, C. Chen, X. Liu, Q. Zhang, Advanced electrode materials in lithium batteries: retrospect and prospect, Energy Mater. Adv. 2021 (2021), 120534.
[4] C. Zhang, A. Wang, J. Zhang, X. Guan, W. Tang, J. Luo, 2D Materials for lithium/sodium metal anodes, Adv. Energy Mater. 8 (2018) 1802833.
[5] R. Xu, X. Cheng, C. Yan, X. Zhang, Y. Xiao, C. Zhao, J. Huang, Q. Zhang, Artificial Interphases for highly stable lithium metal anode, Matter 1 (2019) 317.
[6] J. Ding, R. Xu, X. Ma, Y. Xiao, Y. Yao, C. Yan, J. Huang, Quantification of the dynamic interface evolution in high-efficiency working li-metal batteries, Angew. Chem. Int. Ed. 61 (2022) e202115602.
[7] C. Wang, A. Wang, L. Ren, X. Guan, D. Wang, A. Dong, C. Zhang, G. Li, J. Luo, Controlling li ion flux through materials innovation for dendrite-free lithium metal anodes, Adv. Funct. Mater. 29 (2019) 1905940.
[8] H. Ye, Y. Zhang, Y.X. Yin, F.F. Cao, Y.G. Guo, An Outlook on low-volume-change lithium metal anodes for long-life batteries, ACS Cent. Sci. 6 (2020) 661.
[9] J. Ding, R. Xu, C. Yan, B. Li, H. Yuan, J. Huang, A review on the failure and regulation of solid electrolyte interphase in lithium batteries, J. Energy Chem. 59 (2021) 306.
[10] Z. Cao, Y. Zhang, Y. Cui, J. Gu, Z. Du, Y. Shi, K. Shen, H. Chen, B. Li, S. Yang, Harnessing the unique features of 2d materials toward dendrite-free metal anodes, Energy Environ. Mater. 5 (2021) 45.
[11] Z. Hu, W. Deng, B. He, J. Liang, X. Zhou, Z. Liu, Self-Adaptive 3D Skeleton with charge dissipation capability for practical li metal pouch cells, Nano Energy. 93 (2022), 106805.
[12] S. Gu, S.W. Zhang, J. Han, Y. Deng, C. Luo, G. Zhou, Y. He, G. Wei, F. Kang, W. Lv, Q.H. Yang, Nitrate additives coordinated with crown ether stabilize lithium metal anodes in carbonate electrolyte, Adv. Funct. Mater. 31 (2021) 2102128.
[13] Z. Wen, W. Fang, X. Wu, Z. Qin, H. Kang, L. Chen, N. Zhang, X. Liu, G. Chen, High-concentration additive and triiodide/iodide redox couple stabilize lithium metal anode and rejuvenate the inactive lithium in carbonate-based electrolyte, Adv. Funct. Mater. 2204768 (2022).
[14] W. Ma, Y. Shi, J. Jiang, Y. Xu, X. Liu, C. Shen, Y. Jiang, B. Zhao, J. Zhang, Regulated lithium deposition behavior by chlorinated hybrid solid-electrolyte-interphase for stable lithium metal anode, Chem. Eng. J. 442 (2022), 136297.
[15] S. Li, J. Huang, Y. Cui, S. Liu, Z. Chen, W. Huang, C. Li, R. Liu, R. Fu, D. Wu, A robust all-organic protective layer towards ultrahigh-rate and large-capacity Li metal anodes, Nat. Nanotechnol. 17 (2022) 613.
[16] C. Chen, Q. Liang, G. Wang, D. Liu, X. Xiong, Grain-boundary-rich artificial sei layer for high-rate lithium metal anodes, Adv. Funct. Mater. 32 (2021) 2107249.
[17] Z. Cao, Y. Yang, J. Qin, J. He, Z. Su, 3D TiO_2/ZnO hybrid framework: stable host for lithium metal anodes, Chem. Eng. J. 427 (2022), 132026.
[18] Z. Su, J. Zhang, J. Jin, S. Yang, G. Li, Nanoscale surface modification of polymer nanofibers enables uniform lithium nucleation and deposition for stable lithium metal anodes, Chem. Eng. J. 430 (2022), 132865.
[19] Z. Li, Q. He, C. Zhou, Y. Li, Z. Liu, X. Hong, X. Xu, Y. Zhao, L. Mai, Rationally design lithiophilic surfaces toward high-energy Lithium metal battery, Energy Storage Mater. 37 (2021) 40.
[20] T. Yang, L. Li, T. Zhao, Y. Ye, Z. Ye, S. Xu, F. Wu, R. Chen, From flower-like to spherical deposition: a gcnt aerogel scaffold for fast-charging lithium metal batteries, Adv. Energy Mater. 11 (2021) 2102454.
[21] K. Tantratian, D. Cao, A. Abdelaziz, X. Sun, J. Sheng, A. Natan, L. Chen, H. Zhu, Stable li metal anode enabled by space confinement and uniform curvature through lithiophilic nanotube arrays, Adv. Energy Mater. 10 (2019) 1902819.
[22] Z. Luo, C. Liu, Y. Tian, Y. Zhang, Y. Jiang, J. Hu, H. Hou, G. Zou, X. Ji, Dendrite-free lithium metal anode with lithiophilic interphase from hierarchical frameworks by tuned nucleation, Energy Storage Mater. 27 (2020) 124.
[23] J. Pan, J. Li, H. Dong, Y. Fang, K. Shi, Q. Liu, Achieving Dendrite–free lithium Plating/Stripping from mixed Ion/Electron–Conducting scaffold Li_2S@Ni NWs-NF for stable lithium metal anodes, Chem. Eng. J. 447 (2022), 137401.
[24] X. Huang, X. Feng, B. Zhang, L. Zhang, S. Zhang, B. Gao, P.K. Chu, K. Huo, Lithiated $NiCo_2O_4$ nanorods anchored on 3d nickel foam enable homogeneous li plating/stripping for high-power dendrite-free lithium metal anode, ACS Appl. Mater. Interfaces 11 (2019) 31824.
[25] J. Sun, Y. Cheng, H. Zhang, X. Yan, Z. Sun, W. Ye, W. Li, M. Zhang, H. Gao, J. Han, D.L. Peng, Y. Yang, M.S. Wang, Enhanced cyclability of lithium metal anodes enabled by anti-aggregation of lithiophilic seeds, Nano Lett. 22 (2022) 5874.
[26] D. Li, C. Xie, Y. Gao, H. Hu, L. Wang, Z. Zheng, Inverted anode structure for long-life lithium metal batteries, Adv. Energy Mater. 12 (2022) 2200584.
[27] J. Zheng, Q. Zhao, T. Tang, J. Yin, C. Quilty, G. Renderos, X. Liu, Y. Deng, L. Wang, D. Bock, C. Jaye, D. Zhang, E. Takeuchi, K. Takeuchi, A. Marschilok, L. Archer, Reversible epitaxial electrodeposition of metals in battery anodes, Science 366 (2019).
[28] Y. Fang, R. Lian, H. Li, Y. Zhang, Z. Gong, K. Zhu, K. Ye, J. Yan, G. Wang, Y. Gao, Y. Wei, D. Cao, Induction of planar sodium growth on mxene ($ti_3c_2t_x$)-modified carbon cloth hosts for flexible sodium metal anodes, ACS Nano 14 (2020) 8744.
[29] D. Zhang, S. Wang, B. Li, Y. Gong, S. Yang, Horizontal growth of lithium on parallelly aligned mxene layers towards dendrite-free metallic lithium anodes, Adv. Mater. 31 (2019) e1901820.
[30] D. Yang, C. Zhao, R. Lian, L. Yang, Y. Wang, Y. Gao, X. Xiao, Y. Gogotsi, X. Wang, G. Chen, Y. Wei, Mechanisms of the planar growth of lithium metal enabled by the 2d lattice confinement from a $ti_3c_2t_x$ mxene intermediate layer, Adv. Funct. Mater. 31 (2021) 2010987.

[31] L. Luo, J. Li, H. Yaghoobnejad Asl, A. Manthiram, A 3D lithiophilic mo$_2$n-modified carbon nanofiber architecture for dendrite-free lithium-metal anodes in a full cell, Adv. Mater. 31 (2019) e1904537.
[32] G. Ma, Z. Wang, B. Gao, T. Ding, Q. Zhong, X. Peng, J. Su, B. Hu, L. Yuan, P.K. Chu, J. Zhou, K. Huo, Multilayered paper-like electrodes composed of alternating stacked mesoporous Mo_2N nanobelts and reduced graphene oxide for flexible all-solid-state supercapacitors, J. Mater. Chem. A 3 (2015) 14617.
[33] H. Jin, X. Liu, Y. Jiao, A. Vasileff, Y. Zheng, S. Qiao, Constructing tunable dual active sites on two-dimensional C_3N_4@MoN hybrid for electrocatalytic hydrogen evolution, Nano Energy 53 (2018) 690.
[34] G. Kresse, J. Furthmuller, Efficiency of ab-initio total energy calculations for metals and semiconductors using a plane-wave basis set, Comp. Mater. Sci. 6 (1) (1996) 15–50.
[35] J.P. Perdew, K. Burke, M. Ernzerhof, Generalized gradient approximation made simple, Phys. Rev. Lett. 77 (18) (1996) 3865.
[36] G. Kresse, D. Joubert, From ultrasoft pseudopotentials to the projector augmented-wave method, Phys. Rev. B 59 (3) (1999) 1758–1775.

Supporting Information

Lithiophilic and conductive framework of 2D MoN nanosheets enabling planar lithium plating for dendrite-free and minimum-volume-change lithium metal anodes

De Gao [a], Shuzhen Deng [a, b], Xiaogang Li [c], Yingxi Zhang [a,e], Tuan Lv [a], Yang He [a], Weijian Mao [a], Hui Yang [c], Jingwei Zhang [d], Paul K Chu [e], Kaifu Huo [a,*]

[a] Wuhan National Laboratory for Optoelectronics (WNLO), School of Optical and Electronic Information, Huazhong University of Science and Technology, Wuhan 430074, China.

[b] China-EU Institute for Clean and Renewable Energy, Huazhong University of Science and Technology, Wuhan 430074, China.

[c] Department of Mechanics, School of Aerospace Engineering, Huazhong University of Science and Technology, Wuhan 430074, China.

[d] National & Local Joint Engineering Research Center for Applied Technology of Hybrid Nanomaterials, Henan University, Kaifeng 475004, China

[e] Department of Physics, Department of Materials Science and Engineering, and Department of Biomedical Engineering, City University of Hong Kong, Tat Chee Avenue, Kowloon, Hong Kong, China

[*] Corresponding authors, E-mail: kfhuo@hust.edu.cn

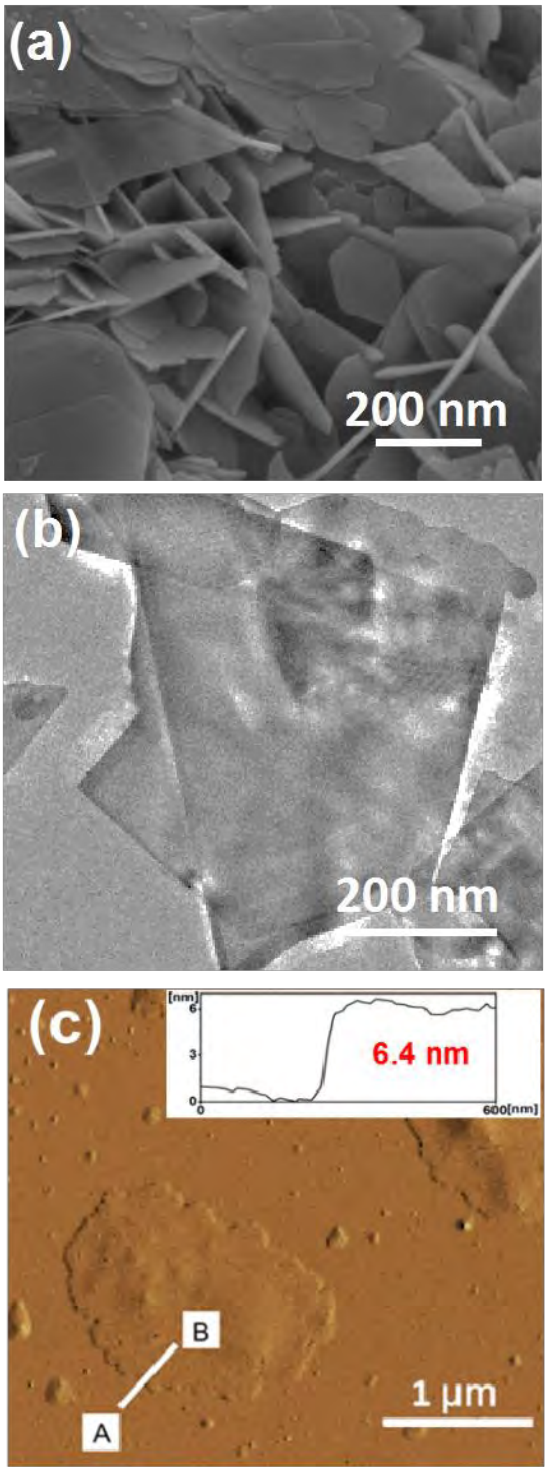

Fig. S1. (a) SEM image, (b) TEM image, and (c) AFM images of the MoN nanosheets.

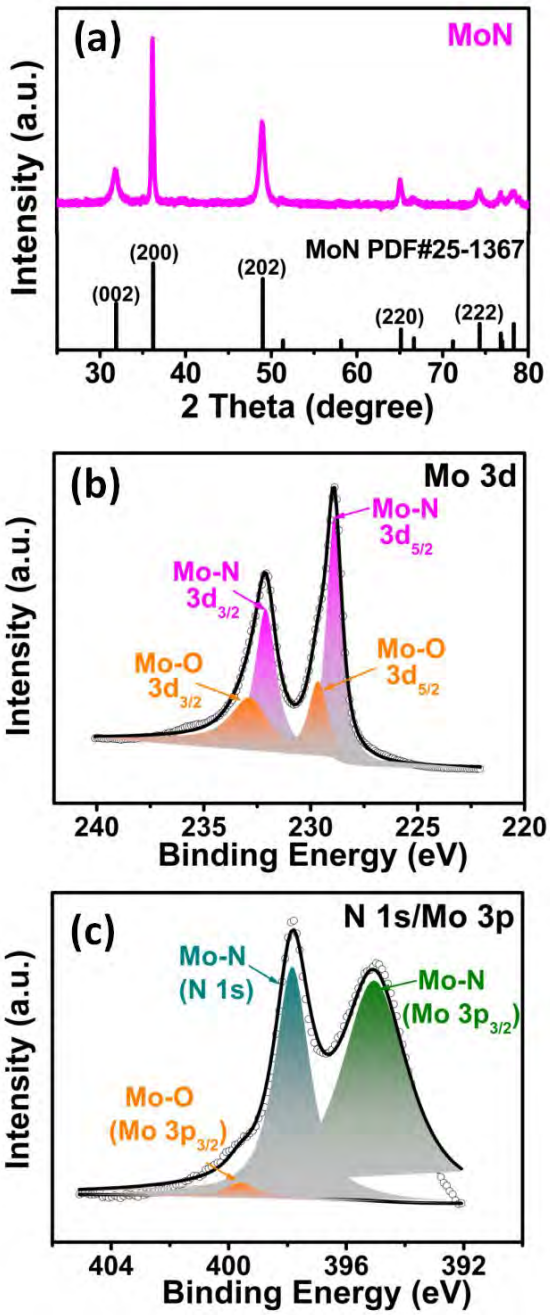

Fig. S2. (a) XRD pattern of MoN nanosheets and high-resolution XPS spectra of (b) Mo 3*d* and (c) N 1*s* / Mo 3*p* of MoN nanosheets.

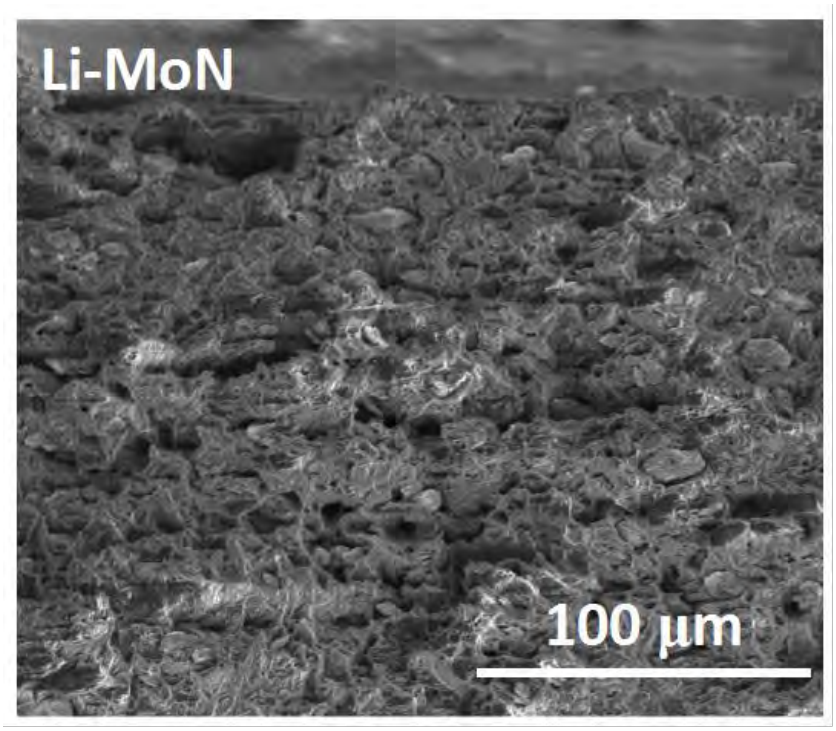

Fig. S3. Cross-sectional SEM image of the Li-MoN film electrode.

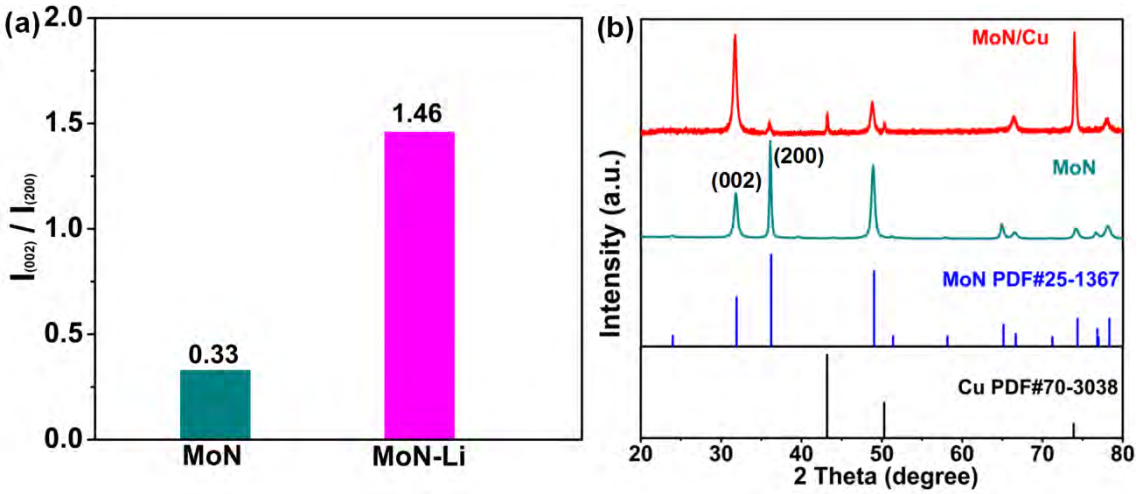

Fig. S4. (a) The ratio of $I_{(002)}/I_{(200)}$ of MoN nanosheet powder and Li-MoN anode, (b) XRD pattern of the MoN/Cu foil.

.

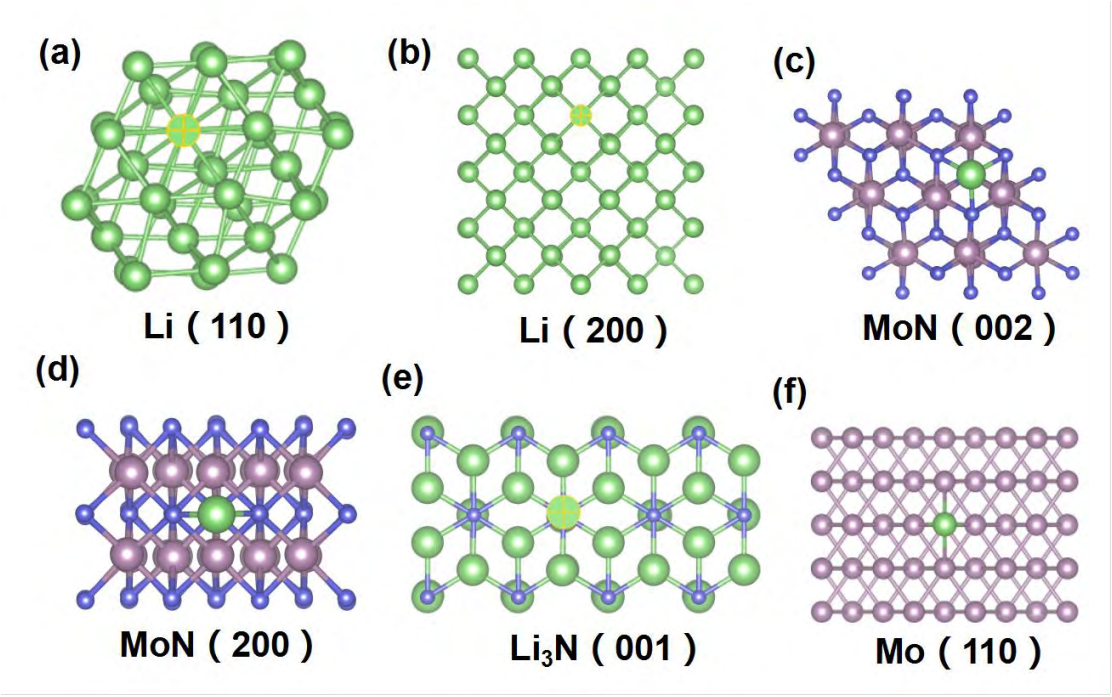

Fig. S5. (a-f) Calculation of the adsorption energy of Li atom on different planes of Li, MoN, Li_3N, and Mo.

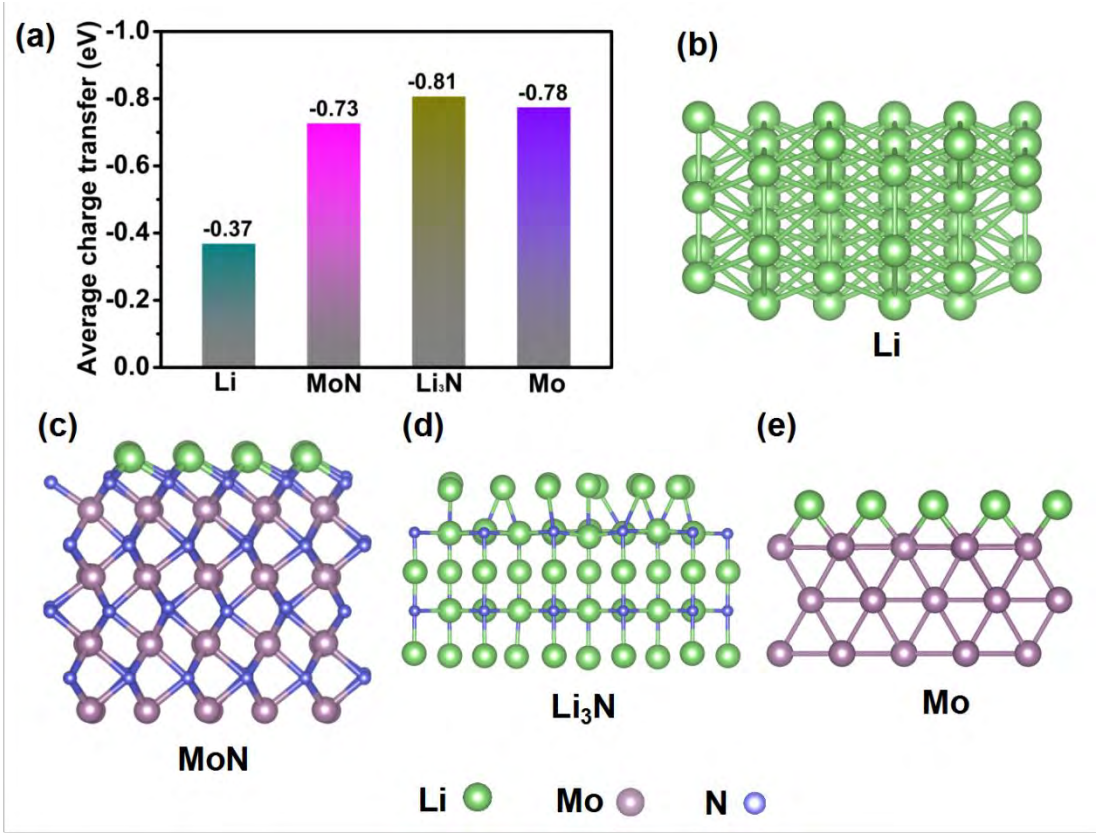

Fig. S6. (a-e) Bader charge analysis of the Li monolayer on different substrate slabs of Li, MoN, Li_3N, and Mo.

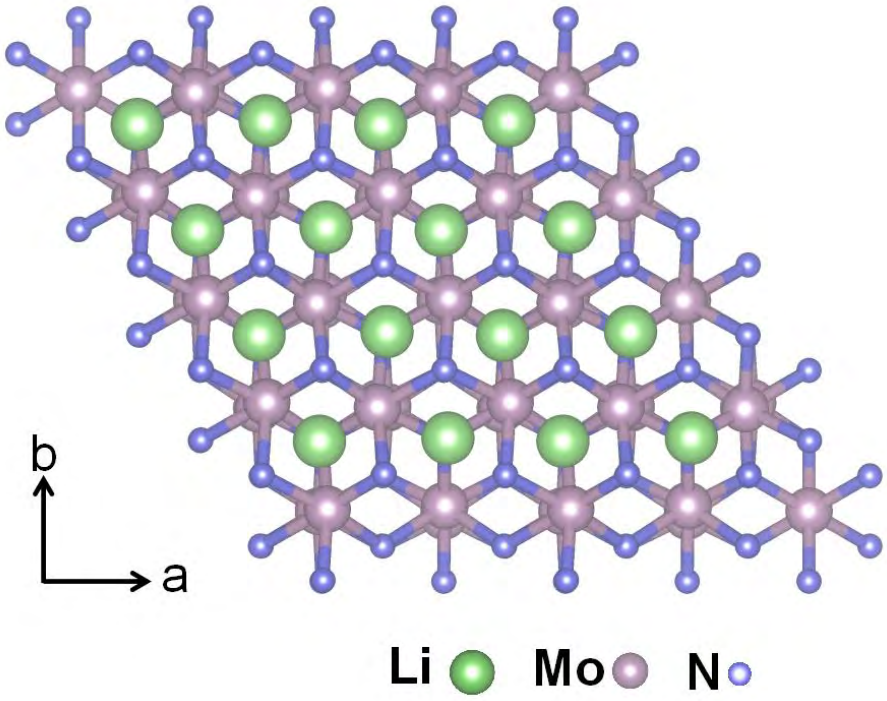

Fig. S7. Schematic showing the lattice mismatch of MoN / hcp−Li.

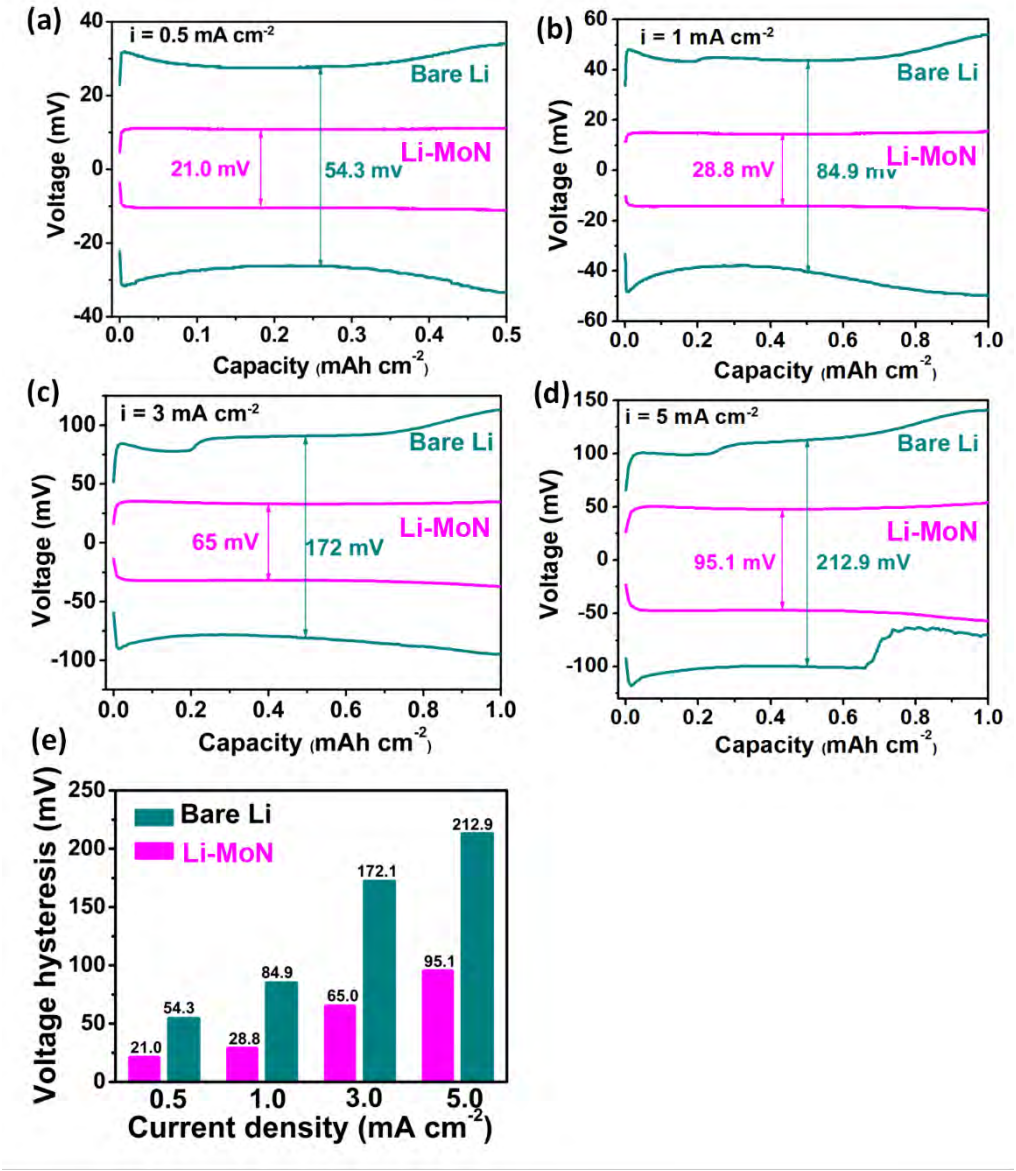

Fig. S8. Voltage profiles (corresponding to Figure 3e) of the symmetrical cells of Li-MoN and bare Li at current densities of (a) 0.5, (b) 1, (c) 3 and (d) 5.0 mA cm^{-2}; (e) Histogram of the voltage hysteresis of the symmetrical cells of Li-MoN and bare Li at different current densities.

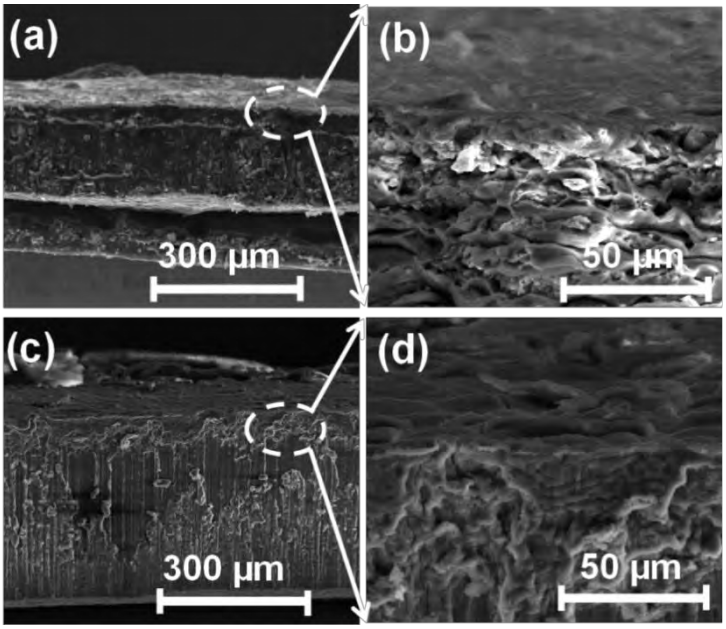

Fig. S9. Cross-sectional SEM images of the Li-MoN film electrode: (a and b) Bare Li electrode and (c and d) after 30 cycling.

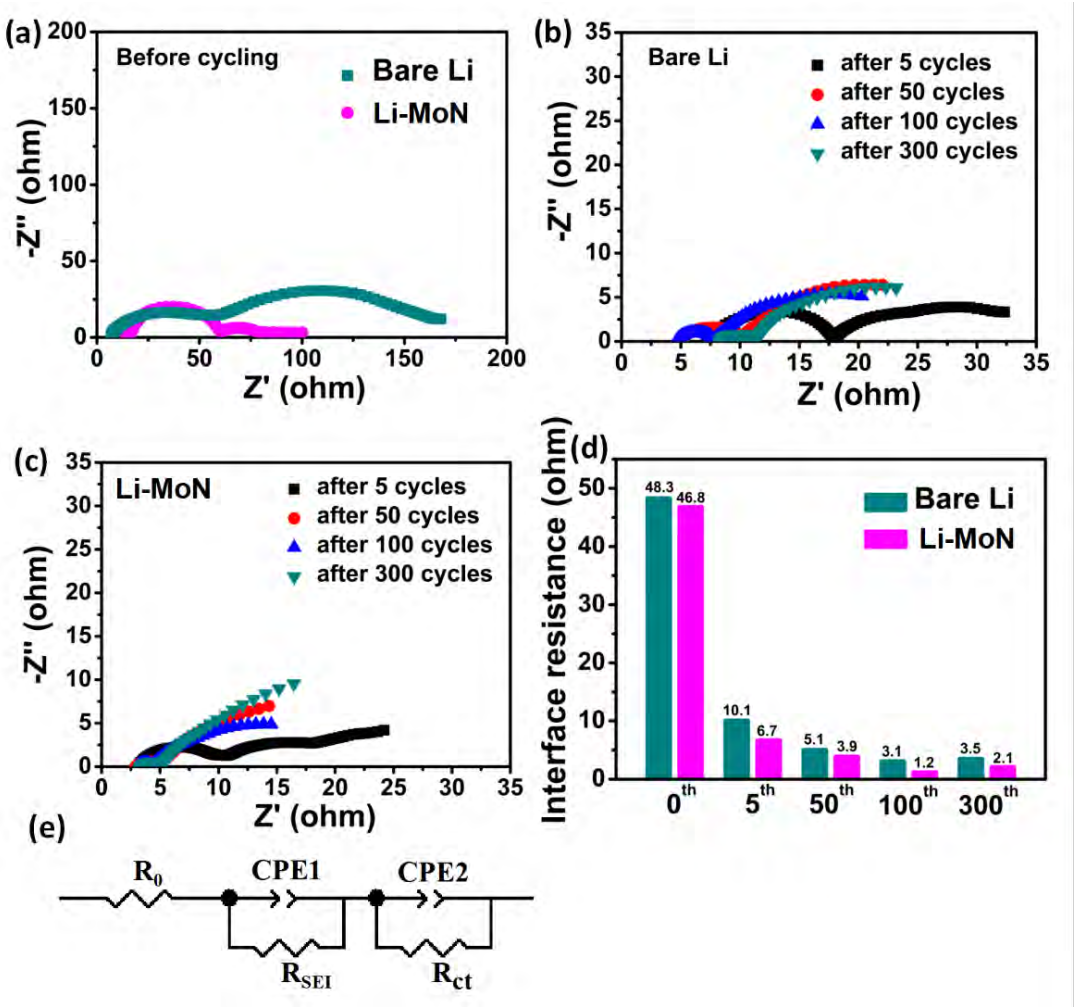

Fig. S10. (a) - (d) EIS curves of the symmetrical cells of Li-MoN and bare Li electrodes after different charging/discharging cycles and (e) Equivalent circuit.

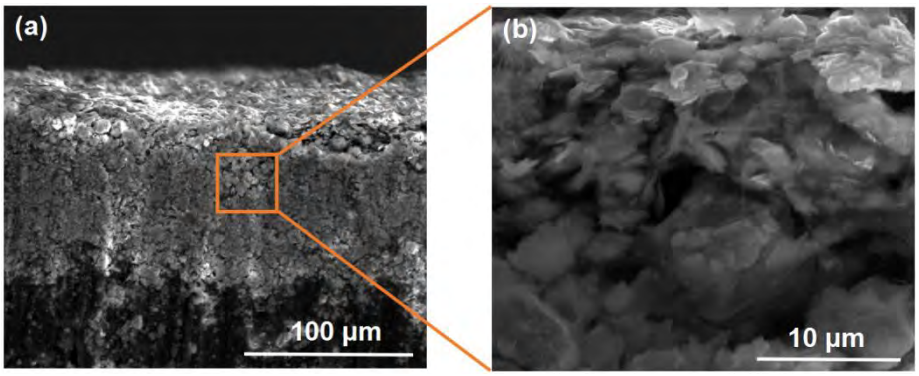

Fig. S11. The cross-sectional SEM images of Li-MoN anode after Li stripping of 12 mAh cm^{-2}.

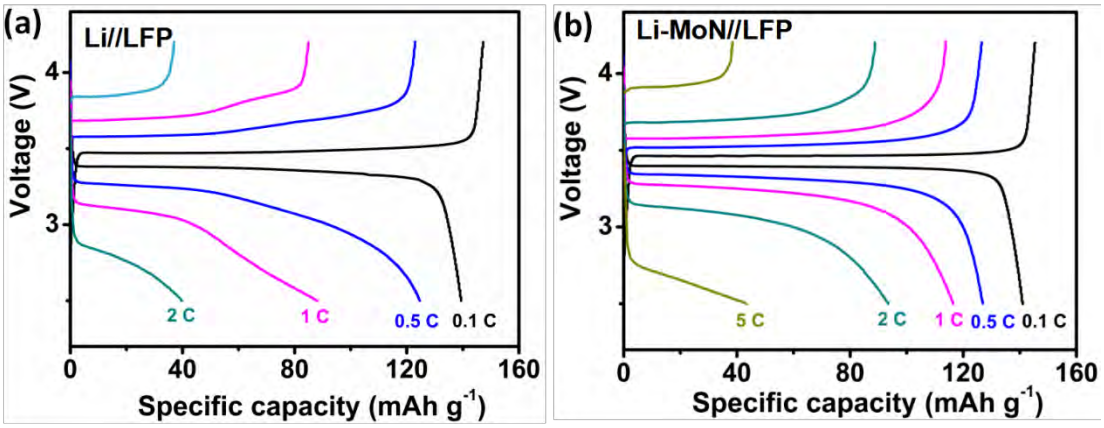

Fig. S12. Voltage profiles of the full cells with (a) Bare Li and (b) Li-MoN as anodes at different current densities.

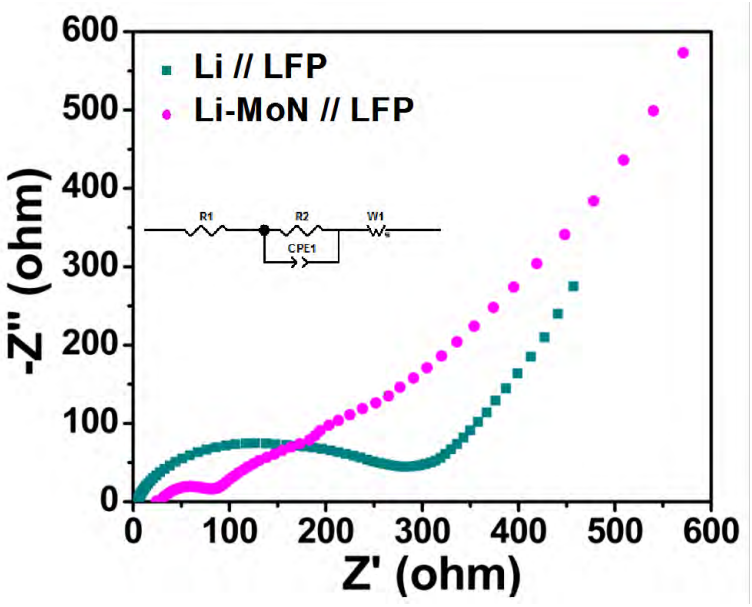

Fig. S13. EIS curves of the LFP full cells with Li-MoN and bare Li anodes after the rate test.

Table S1. Comparison between MoN and hcp−Li.

Li-p6$_3$/mmc	MoN-p6$_3$/mmc	MoN / hcp−Li Lattice Mismatch
d_a-3.07 Å	d_a-3.02 Å	δa-1.6%
d_b-5.31 Å	d_b-5.07 Å	δa-4.5%

The atomic distances between two adjacent Li atoms (N atoms or Mo atoms for MoN) in the d_a and d_b are determined to evaluate the lattice mismatch between hcp Li and MoN The results demonstrate that the lattice mismatch of MoN/hcp−Li is 1.6% and 4.5% in the direction the of a and b axis.